Desorption of oxygen from $YBa_2Cu_3O_{6+x}$ films studied by Raman spectroscopy

A. Bock, R. Kürsten, M. Brühl, N. Dieckmann, and U. Merkt
Institut für Angewandte Physik und Zentrum für Mikrostrukturforschung, Universität Hamburg, Jungiusstraße 11, D-20355 Hamburg, Germany
(Received 1 February 1996)

Phonons of laser-deposited $YBa_2Cu_3O_{6+x}$ films on MgO(100) substrates are investigated in a Raman setup as a function of laser power density. Investigations of $YBa_2Cu_3O_7$ films allow us to study oxygen out-diffusion, where the onset of out-diffusion is indicated by the appearance of disorder-induced modes in the Raman spectra. At a pressure of 5×10^{-6} mbar the temperature threshold of the out-diffusion is (490 ± 15) K. With increasing oxygen pressure the observed temperature thresholds rise only moderately in contrast to the behavior expected from the p_{ox}-T phase diagram of $YBa_2Cu_3O_{6+x}$. Even at 1 bar oxygen partial pressure out-diffusion is observed and tetragonal sites with $x=0$ develop. These observations can be explained by photon-stimulated desorption of oxygen. Investigations of $YBa_2Cu_3O_6$ films allow us to study oxygen in-diffusion. In 1 bar oxygen we observe competing oxygen fluxes due to thermally activated diffusion and photon-stimulated desorption. From these measurements we determine an upper bound of the thermal activation energy of the oxygen in-diffusion into $YBa_2Cu_3O_6$ films of (0.19 ± 0.01) eV. [S0163-1829(96)02730-0]

I. INTRODUCTION

$YBa_2Cu_3O_{6+x}$ ($YBCO_{6+x}$) is one of the most prominent high-temperature superconductors. In addition to the well-known CuO_2 planes, which are common for all high-T_c compounds, it posesses Cu(1)-O(1) chains. These chains serve as a doping reservoir for the CuO_2 planes, where the superconducting coupling is believed to take place.[1] The chain-oxygen content x determines the superconducting properties of $YBCO_{6+x}$, where a maximum transition temperature $T_{c,0}=91$ K is observed at $x=0.88$.[2] The chain-oxygen content is a function of sample temperature and oxygen partial pressure.[3] At a given temperature, the chain oxygen O(1) has the highest mobility of all the oxygen sites.[4] Already at room temperature surface degradations with long time scales, which are most likely due to oxygen out-diffusion from chain sites, have been observed under UHV conditions.[5] Additionally, it has been shown that the chain oxygen migrates in high electric fields[6] and that radiation-induced oxygen loss at the chain site occurs when $DyBCO_7$ samples are investigated with synchrotron radiation of high intensity.[7] The oxygen loss in the latter experiment has been assigned to photon-stimulated desorption of oxygen, with an energy threshold for the desorption of about 15 eV. It is well known that laser beams of high intensity can be used to pattern $YBCO_{6+x}$ films by writing or rewriting oxygen-depleted areas using low or high oxygen partial pressures, respectively.[8] Whether or not photon-stimulated desorption of oxygen plays an important role in this processes in the visible regime as well has not been investigated so far.

Here we present laser-annealing measurements of $YBCO_{6+x}$ films on MgO(100) substrates using photon energies of 2.41, 2.58, and 2.71 eV and high power densities. In these measurements the laser serves the dual role of heating and investigating the film simultaneously as the measurements are performed in a Raman setup.[9] The Raman spectra are used to determine the oxygen content and the temperature in the laser spot. We believe that these Raman spectra give evidence that already at 2.41 eV photon-stimulated desorption of oxygen in $YBCO_{6+x}$ films occurs.

This paper is organized as follows. After the description of experimental details in Sec. II we present a representative laser-annealing measurement of a $YBCO_7$ film in Sec. III. Following the description of laser-induced heating of $YBCO_7$ films in Sec. IV we investigate the oxygen out-diffusion mechanism at low residual pressures in Sec. V. In Sec. VI we describe the results of laser-annealing measurements of $YBCO_7$ films at high residual pressures up to 1 bar oxygen. Furthermore, we show measurements of a tetragonal $YBCO_6$ film in 1 bar oxygen. Micro-Raman investigations of laser-annealed sites of the tetragonal film reveal that only a ring of $YBCO_{6.5}$ develops under these conditions while the center remains tetragonal. In Sec. VII we discuss our observations in terms of thermally activated diffusion and photon-stimulated desorption of oxygen.

II. EXPERIMENTAL DETAILS

We investigate c-axis-oriented $YBCO_7$ films on MgO(100) substrates prepared by laser deposition.[10] The films are typically more than 200 nm thick and exhibit critical temperatures $T_{c,0}$ between 83 K and 89 K. Their critical current densities j_c at 77 K are around 10^6A cm^{-2}. The films are mounted on the cold finger of a liquid helium cryostat which can be evacuated to residual pressures $p=5\times10^{-6}$ mbar. The cryostat temperature T_0 is measured by a silicon diode and coincides with the film temperature in the absence of illumination. Calibrated and straylight-corrected Raman spectra are taken in quasibackscattering geometry in a Dilor XY-Raman spectrometer equipped with a multichannel diode-array detector and a Princeton Instruments CCD camera, type LN 1100 PB/VISAR. Details of the calibration and the straylight correction are given elsewhere.[9] We use the Porto notation $z(x,x)\overline{z}$ to describe the spectra. Here the first and last letters represent the directions of the incoming and scattered photons with respect to the crystal axes of the

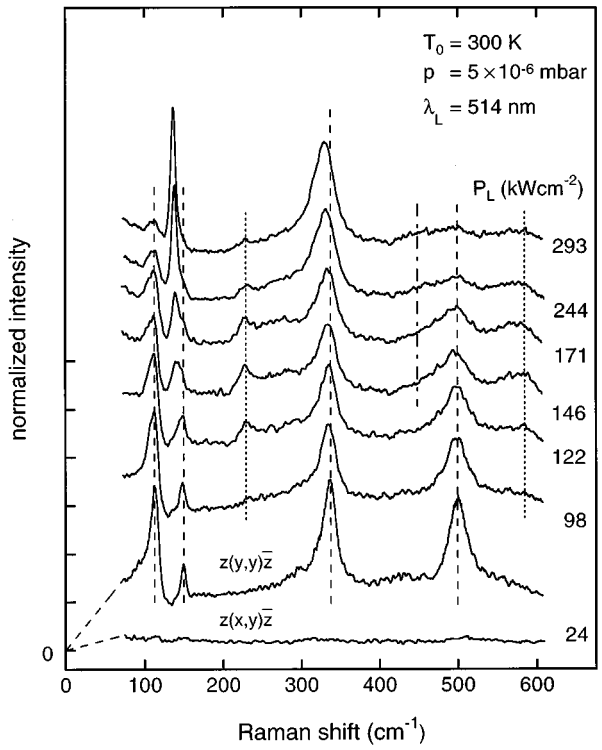

FIG. 1. Polarized Stokes Raman spectra of a laser-annealing measurement for different power densities P_L with an effective spot radius $r_e = 8.4$ μm. Also depicted is a depolarized spectrum taken at the lowest power density $P_L = 24$ kW cm^{-2}. The spectra are offset as indicated and their intensities are normalized with respect to the power density. The dashed lines correspond to the A_g phonons of $YBCO_7$, dotted lines to infrared-active modes of $YBCO_{6.5}$, and the dash-dotted line to the O(2)+O(3) mode of $YBCO_6$.

sample whereas the letters in brackets denote the incoming and scattered polarizations. As the films are heavily twinned we cannot distinguish between the x and y polarizations of the Raman signal. We therefore use x and y to distinguish polarizations perpendicular and parallel to the entrance slit of the spectrometer when they are parallel to the crystal axes of the substrate. Given the laser power of the Gaussian spot on the sample P, the maximum power density is $P_L = P/(\pi r_h r_v)$. Here r_h and r_v are the $(1/e)$ radii of the laser focus in horizontal and vertical directions, respectively. The radii are determined from the spot profile measured for each laser line. The effective spot area is described by πr_e^2, with $r_e = \sqrt{r_h r_v}$. In the following we will call P_L the ''power density.'' From an analysis of spectra at low power density we obtain the epitaxial quality and the oxygen content of the films. In these spectra the following A_g modes are visible at 300 K (see, e.g., the polarized spectrum at $P_L = 24$ kW cm^{-2} in Fig. 1): the Ba mode at 120 cm^{-1}, the Cu(2) mode at 150 cm^{-1}, the out-of-phase plane oxygen mode O(2)-O(3) at 340 cm^{-1}, and the apex oxygen mode O(4) at 500 cm^{-1}.[11] The spectra are fitted using Fano profiles for the Ba and the O(2)-O(3) mode, Lorentz profiles for the Cu(2) and the O(4) mode, and an almost constant background. Comparison of the intensities of the O(2)-O(3) modes and the O(4) modes in polarized and depolarized spectra allows us to determine the epitaxy parameters of the film.[12] The orthorhombic $YBCO_7$ film investigated here has a c-axis-oriented fraction of $(94\pm5)\%$ and an in-plane orientation of this fraction of $(89\pm5)\%$. The oxygen content of the orthorhombic film turns out to be $x = 0.95\pm0.05$ using the frequency of the O(4) mode and the frequency to oxygen content relation by Feile *et al.*[13] The investigated tetragonal $YBCO_6$ film has an oxygen content of $x = 0.05\pm0.05$ using the frequency of the Cu(2) mode and the frequency to oxygen content relation by Burns *et al.*[14] The thicknesses of both films are 240 nm.

III. EXAMPLE OF A LASER-ANNEALING MEASUREMENT

A laser-annealing measurement is performed in the following way. With increasing power density a series of polarized Stokes and anti-Stokes spectra are taken subsequently at each power density. Before we record the first spectrum we wait about 3 min in order to establish thermal equilibrium. Stokes spectra of a typical measurement performed on a $YBCO_7$ film are presented in Fig. 1. This measurement was carried out with a green argon laser line $\lambda_L = 514$ nm at a low residual pressure $p = 5\times10^{-6}$ mbar. At the lowest power density we observe the four expected A_g phonons of $YBCO_7$. When the power density is increased to values above 96 kW cm^{-2} new modes begin to develop at 230 cm^{-1} and 585 cm^{-1}. Up to a power density of 150 kW cm^{-2} the intensity of these modes grows continuously. At still higher power densities their intensities start to decrease until they almost vanish at the highest power density of 293 kW cm^{-2}. In addition to the above findings, we observe with increasing power density that the Cu(2) and O(2)-O(3) modes rise in intensity, the Ba and the O(4) modes diminish, and other modes appear at 280 cm^{-1} and 450 cm^{-1}. The mode at 230 cm^{-1} and the modes at 280, 450, and 585 cm^{-1} are described using Fano and Lorentz profiles, respectively.

The modes at 230, 280, and 585 cm^{-1} are infrared-active modes of $YBCO_{6+x}$ dominated by vibrations of Cu(1), O(1), and O(4), respectively.[15,16] They become Raman active for $x \approx 0.5$ due to disorder in the occupancy of the chain-oxygen site. Thus, the appearance of these modes indicates the onset of oxygen out-diffusion. The mode at 450 cm^{-1} is a Raman-active plane-oxygen mode O(2)+O(3) of $YBCO_6$.[14] The remaining Raman-active phonons of $YBCO_6$ expected in the applied polarization geometry are the Cu(2) mode at 140 cm^{-1} and the O(2)-O(3) mode at 340 cm^{-1}.[14] These two modes are in fact observed in the spectrum recorded at the highest power density of 293 kW cm^{-2}.

Obviously, with increasing power density oxygen out-diffusion takes place. In a continuous oxygen-desorption process one would expect that the O(4) as well as the Cu(2) mode softens continuously with decreasing oxygen content.[13,14] In contrast, we observe that the frequency of the O(4) mode at 500 cm^{-1} remains almost constant while a shoulder develops on its low-energy side, making it difficult to fit the mode for power densities above 171 kW cm^{-2}. This shoulder may result from a phonon at 485 cm^{-1} which was assigned to the O(4) mode of $YBCO_{6.5}$.[17] Furthermore, the line shape of the Cu(2) mode differs significantly from a Lorentz profile at power densities above 96 kW cm^{-2}. In fact, two or three phonons provide a better description of the spectral range 130–160 cm^{-1}. The resulting frequencies and

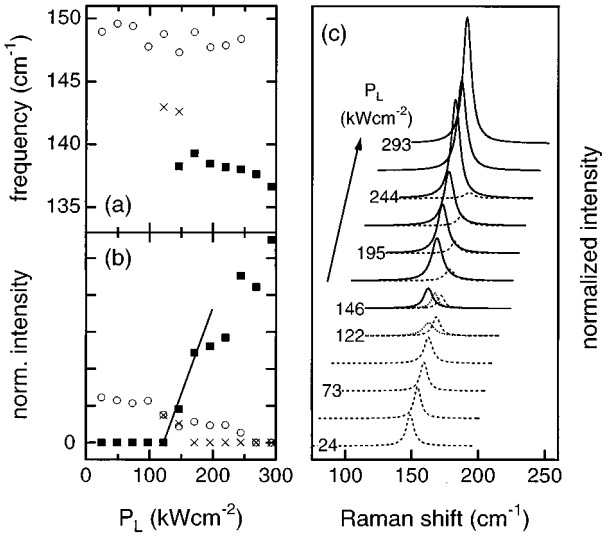

FIG. 2. Frequencies (a) and normalized intensities (b) of the Cu(2) modes in $YBCO_{6+x}$ for $x=1$ (open circles), $x\approx 0.5$ (crosses), and $x=0$ (solid squares). The solid line in (b) represents a straight line which allows us to determine the threshold of the appearance of the Cu(2)-O_6 mode. (c) The individual phonon line shapes. Dashed lines correspond to the Cu(2)-O_7 mode, dotted lines to the 143 cm^{-1} mode, and solid lines to the Cu(2)-O_6 mode. For convenience the spectra are offset and shifted as indicated.

intensities are shown in Figs. 2(a) and 2(b). For power densities above 150 kW cm^{-2} the frequencies almost match the frequencies of the Cu(2) mode in $YBCO_7$ (150 cm^{-1}) and in $YBCO_6$ (140 cm^{-1}). The slight decrease of the phonon frequencies with increasing power density results from increasing spot temperatures which will be discussed in Sec. IV. As shown in Fig. 2(c) we also observe a mode at 143 cm^{-1} which corresponds to an intermediate oxygen content of $x\approx 0.5$ in the measurement recorded at a power density of 146 kW cm^{-2}. This mode is already observed in the two-phonon fit of the 122 kW cm^{-2} measurement with a comparatively large width. With the appearance of infrared-active modes above 96 kW cm^{-2} the intensity of the Cu(2)-O_7 mode decreases. Concomitantly, the intensity of the 143 cm^{-1} mode which originates from regions with $x\approx 0.5$ increases. At power densitites above 150 kW cm^{-2} the 143 cm^{-1} mode can no longer be resolved as the Cu(2)-O_6 mode becomes too strong [see Fig. 2(c)]. The large intensity of the Cu(2)-O_6 mode is correlated with its high Raman efficiency.[18] The threshold of the appearance of the Cu(2)-O_6 mode turns out to be (111 ± 4) kW cm^{-2}.

An optical micrograph of the laser-annealed site is depicted in Fig. 3(a). The oxygen-depleted regions appear brighter because of their higher reflectivities.[6] Due to thermal expansion of the cold finger during the laser-annealing measurement, the spot has moved on the film from the upper right corner to the lower center of the micrograph. We have performed micro-Raman measurements in ambient atmosphere at the sites labeled 1–5. Representative spectra are shown in Fig. 3(b). From the measurements we have determined the local oxygen content x using the frequencies of the O(4) and Cu(2) modes. It turns out that the dark and bright areas have oxygen contents close to $x=1$ and $x=0$,

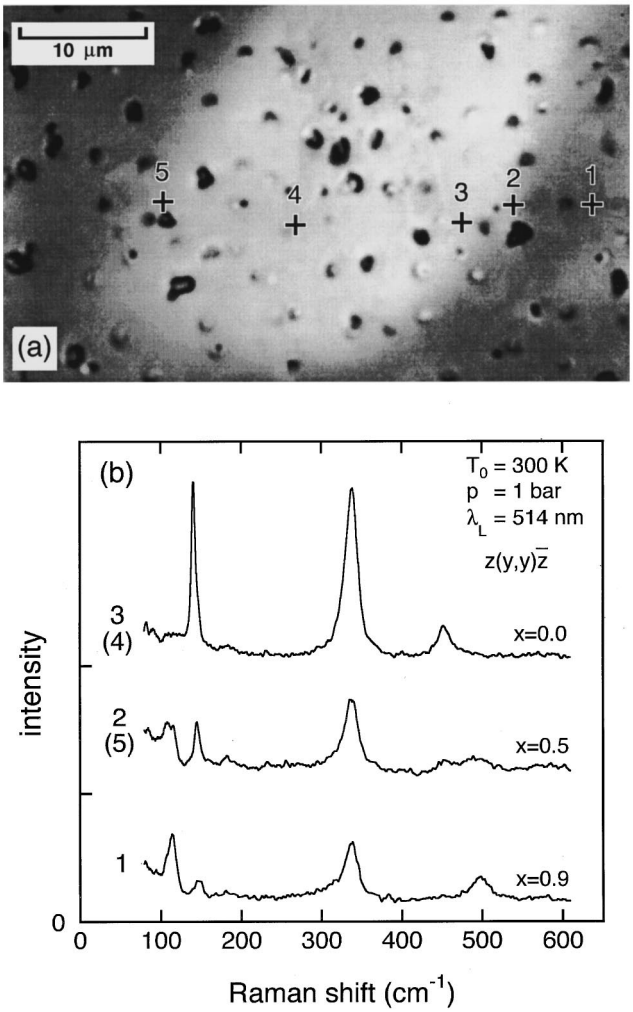

FIG. 3. (a) Optical micrograph of a $YBCO_7$ film after a laser-annealing measurement. Dark and bright areas correspond to $x\approx 1$ and $x=0$, respectively. The spots are precipitates on the film surface; see Ref. 19. Crosses 1 – 5 mark sites where the polarized micro-Raman spectra (b) have been taken with a power density $P_L=65$ kW cm^{-2} and an effective spot radius $r_e=0.9\mu$m. The spectra are offsets as indicated. Spectra taken at sites 4 and 5 are almost identical to the spectra of sites 3 and 2, respectively.

respectively. Only in a narrow region between both areas, which is at most 5 μm wide, is an oxygen content $x=0.5$ observed. This oxygen content corresponds to the second orthorhombic phase $YBCO_{6.5}$. From both the line shape analysis in Fig. 2 which leads to separate Cu(2) modes and the micro-Raman measurements which reveal a steep transition from $x\approx 1$ to $x=0$ we conclude that the spot area consists of regions where either $x\approx 1$ or $x=0$ is stable, separated by a narrow region with an intermediate oxygen content $x\approx 0.5$ which gives rise to the disorder-induced modes. At room temperature the chain oxygen in the narrow region rearranges into the second orthorhombic phase $YBCO_{6.5}$. Except for measurements at 98 kW cm^{-2} we did not observe significant changes of the spectra when we recorded a second Stokes spectrum after about 15 min. Thus, the irradiated spot must have reached its equilibrium oxygen distribution already before the first Stokes spectrum was taken, i.e., 3 min after the power density was adjusted.

IV. DESCRIPTION OF LASER HEATING

The heat flow introduced by the absorbed laser light generates temperature increases in the film $\Delta_f(r)$, across the film-substrate boundary $\Delta_b(r)$, and in the substrate $\Delta_s(r)$. The temperature increases in the center of the laser spot define the maximum spot temperature

$$T_{\max}=\Delta_f(0)+\Delta_b(0)+\Delta_s(0)+T_0. \quad (1)$$

The temperature increases can be calculated according to Eq. (4) of Ref. 9. They are proportional to the power density P_L and are mainly a function of the film thickness h, the penetration depth l, the effective spot radius r_e, the reflectivity R, and the thermal conductivities of film and substrate, κ_f and κ_s, as well as of the thermal boundary resistance of the film-substrate interface $R_{\rm bd}$. In our calculations the penetration depth and the reflectivity are taken from the literature.[20] While the thermal conductivity data can be taken from the literature as well,[9,21,22] we have determined the thermal boundary resistance $R_{\rm bd}=(0.5\pm0.1)\times10^{-3}$ kW cm^{-2} of the investigated film as described elsewhere.[9]

For a laser-heated crysal the lateral distribution of the temperature increase at the surface in the limit of great attenuation $W=r_e/l$ can be described by[23]

$$\Delta_{\rm crystal}(r)=\Delta_{\max}N(R,Z=0,W=\infty), \quad (2)$$

with

$$N(R,Z=0,W=\infty)=\frac{1}{\sqrt{\pi}}\int_0^\infty J_0(\lambda R)\exp\left(-\frac{\lambda^2}{4}\right)d\lambda, \quad (3)$$

where $\Delta_{\max}$ is the maximum temperature increase of the illuminated crystal, $N(R,Z=0,W=\infty)$ is a normalized function,[23] and $R=r/r_e$ and $Z=z/r_e$ are coordinates which are normalized with respect to the effective spot radius. $J_0(\lambda R)$ is the Bessel function of zero order. In order to describe the lateral temperature distribution of the film-substrate system we replace, in Eq. (2), $\Delta_{\max}$ by $\Delta_f(0)$ and $\Delta_s(0)$ for the film and the substrate, respectively. The lateral temperature distribution at the film-substrate interface is described by a Gaussian with maximum $\Delta_b(0)$ which is a consequence of the boundary conditions.[9] In the following $T_{\max}(r)$ describes the lateral temperature distribution at the film surface. Given this temperature distribution we can calculate the Stokes–anti-Stokes spot temperature $T_{S/AS}$ visible in Raman experiments by integrating the lateral intensity and temperature distributions. We obtain the relation

$$T_{S/AS}=T_0+\frac{1}{\sqrt{2}}[\Delta_f(0)+\Delta_s(0)]+\frac{1}{2}\Delta_b(0). \quad (4)$$

Here we have neglected the vertical temperature distribution within the penetration depth as the temperature varies only little there.[23] The experimental spot temperature is determined from a comparison of Stokes and anti-Stokes intensities according to Eq. (10) of Ref. 9. It is worthwhile to mention that the lateral temperature distribution according to Eq. (3) falls off parabolically close to the center and as $(1/r)$ far from the spot area.

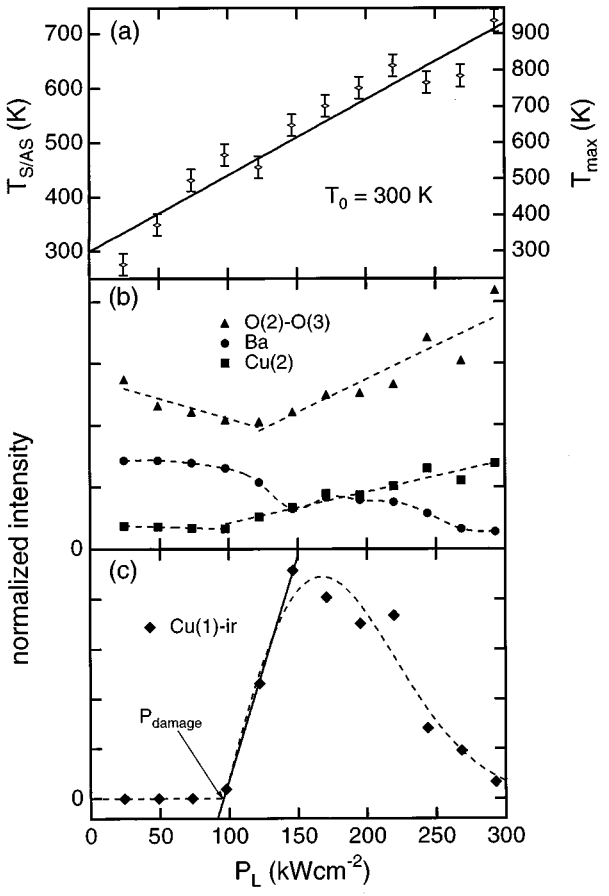

FIG. 4. (a) Spot temperatures $T_{S/AS}$ versus power density. The temperatures are determined from Stokes and anti-Stokes spectra of the laser-annealing measurement partially depicted in Fig. 1. The solid line represents the Stokes–anti-Stokes spot temperature calculated according to Eq. (4). Also given are the maximum spot temperatures calculated according to Eq. (1). Normalized intensities of the Raman-active modes (b) and of the Cu(1)-ir mode (c) are also given. The solid line in (c) represents a straight line which allows us to determine the damage threshold $P_{\rm damage}$. Dashed lines are guides to the eye.

V. LASER ANNEALING AT LOW RESIDUAL PRESSURES

In Fig. 4(a) we present experimental and calculated spot temperatures for the laser-annealing measurement of Fig. 1. Within the error bars the temperatures are in good agreement. Also given are calculated maximum spot temperatures $T_{\max}$. In Fig. 4(b) normalized intensities of three Raman-active phonons are depicted. The intensities are normalized with respect to the power density. We have not included the O(4) mode because its intensity cannot be fitted with high accuracy for power densities above 171 kW cm^{-2}. In Fig. 4(c) we show normalized intensities of the Cu(1)-ir mode which behave similar to the intensities of the O(4)-ir mode not shown here.

At power densities below 100 kW cm^{-2}, the normalized intensities of the Ba and the Cu(2) modes remain constant whereas the O(2)-O(3) mode shows a slight decrease of its intensity. This is a consequence of the temperature dependence of its Raman efficiency.[24] The variations of the intensities of the Raman-active modes above 100 kW cm^{-2} are related to the onset of oxygen out-diffusion and the change

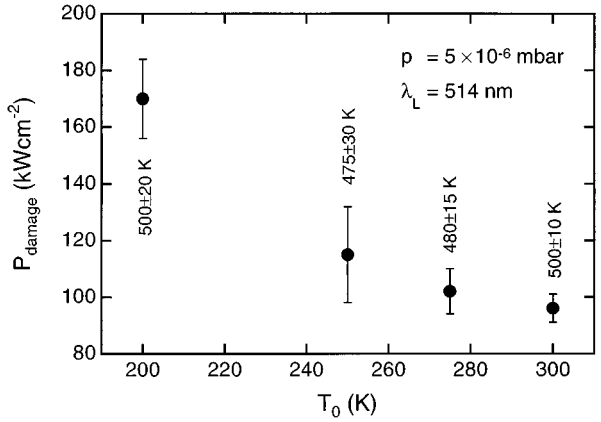

FIG. 5. Damage thresholds vs cryostat temperature. The corresponding maximum spot temperatures $T_{\max}$ are indicated. The effective spot radius is $r_e = 8.4\ \mu$m.

of Raman efficiencies with oxygen content.[18,25] A straight-line fit to the intensity of the Cu(1)-ir mode up to 150 kW cm^{-2} allows us to determine the power density where the mode starts to develop. We will call this value the ''damage threshold'' P_{damage} in the following. Also we will use the spot temperatures calculated from the heat model in the discussion of the oxygen out-diffusion.

We have carried out similar laser-annealing measurements at cryostat temperatures $T_0 = 200$, 250, and 275 K and a residual pressure $p = 5 \times 10^{-6}$ mbar. Due to the weak temperature dependence of the thermal conductivities and the thermal boundary resistance,[22,26] the cryostat temperature has only little influence on the temperature increases in this temperature range. In Fig. 5 we depict the damage thresholds and the concomitant maximum spot temperatures for these measurements. Apparently, the damage thresholds increase with decreasing cryostat temperature. However, the corresponding maximum spot temperatures remain almost constant. From this we conclude that the oxygen out-diffusion mechanism is mainly temperature induced when the laser annealing is done at a low residual pressure. The mean value of the temperature threshold where desorption of oxygen occurs is $T_{k1} = (490 \pm 15)$ K. The threshold of complete desorption of the chain oxygen, T_{k2}, is determined by the appearance of the Cu(2)-O_6 mode as shown in Fig. 2. We find this second threshold at $T_{k2} = (580 \pm 20)$ K. Taking also into account the results presented in Sec. III we have developed the following picture in order to describe the oxygen-desorption process: Oxygen out-diffusion occurs only in areas whose temperature exceeds the temperature threshold T_{k1}. Unless the local temperature does not exceed the threshold of complete oxygen desorption, T_{k2}, these areas can be described by an intermediate oxygen content $x \approx 0.5$. Areas whose local temperatures exceed the second threshold T_{k2} are tetragonal ($x = 0$).

As described in Sec. IV we can calculate the lateral temperature profile at the surface of an illuminated $YBCO_7$ film. Knowledge of this temperature profile allows us to determine the radius $r_T(P_L)$ of a given temperature T as a function of the power density. Results of such a calculation are presented in Fig. 6(a) for temperatures which correspond to the temperature thresholds T_{k1} and T_{k2} of the 300-K laser-annealing

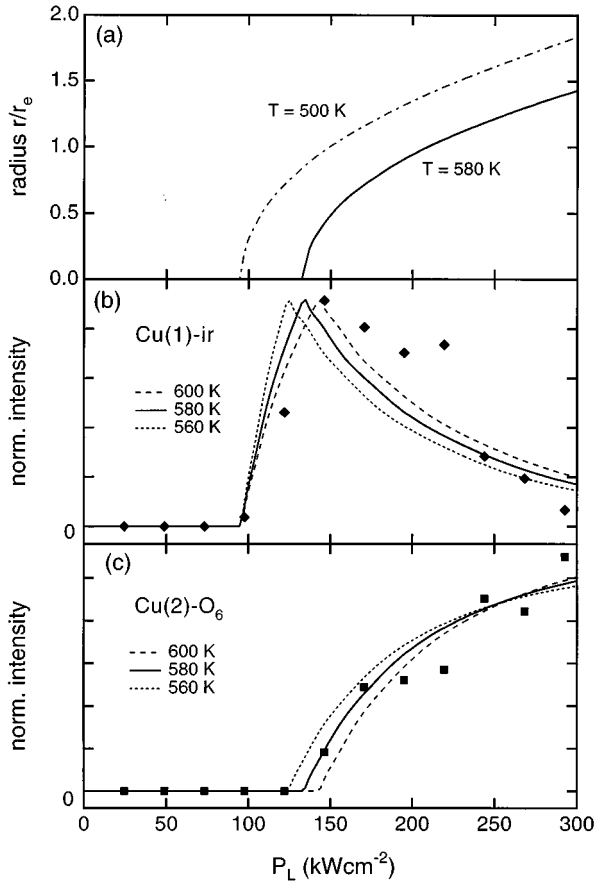

FIG. 6. (a) Radii of constant temperature $T = 500$ K and $T = 580$ K vs power density. The radii are normalized with respect to the effective spot radius $r_e = 8.4\ \mu$m. Normalized intensities of the Cu(1)-ir mode (b) and the Cu(2)-O_6 mode (c) are also given. Solid symbols represent measured data and the lines correspond to intensities calculated according to Eq. (5) with $T_{k1} = 500$ K and different T_{k2} as indicated.

measurement depicted in Fig. 1. As we can neglect the vertical temperature profile of the film within the penetration depth, we can calculate the variation of the intensities of the Cu(1)-ir mode and of the Cu(2)-O_6 mode using the Gaussian distribution of the power density. We obtain

$$I_{\text{Cu(1)-ir}}(P_L) = I_{\text{Cu(1),0}} \left\{ \exp\left[-\frac{r^2_{T_{k2}}(P_L)}{r_e^2} \right] - \exp\left[-\frac{r^2_{T_{k1}}(P_L)}{r_e^2} \right] \right\}, \tag{5a}$$

$$I_{\text{Cu(2)-O}_6}(P_L) = I_{\text{Cu(2),0}} \left\{ 1 - \exp\left[-\frac{r^2_{T_{k2}}(P_L)}{r_e^2} \right] \right\}, \tag{5b}$$

where $I_{\text{Cu(1),0}}$ and $I_{\text{Cu(2),0}}$ are intensities used as fit parameters. In the above equation we use $r_{T_{kj}}(P_L) \equiv 0$ for $T_{\max}(P_L) \leqslant T_{kj}$, $j = 1,2$. Comparison of calculated intensities with measured data [see Figs. 2(b) and 4(b)] are shown in Figs. 6(b) and 6(c). The agreement between experiment and calculation is fairly good although we have neglected the effect of lateral oxygen diffusion on the local oxygen con-

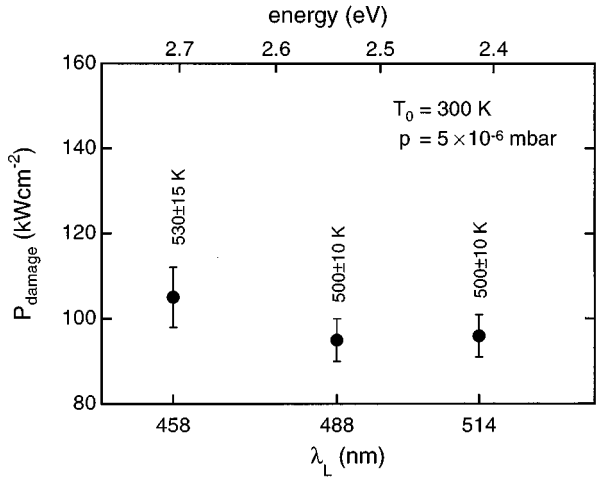

FIG. 7. Damage thresholds vs excitation wavelength. The corresponding maximum spot temperatures $T_{\max}$ are indicated. The effective spot radius is $r_e = 8.4\ \mu$m.

tent. Furthermore, it turns out that the observed inner radius is in good agreement with the calculated one [see Fig. 3(a)].

We have also performed laser-annealing measurements using wavelenghts $\lambda_L = 488$ nm and $\lambda_L = 458$ nm. The results of these measurements are depicted in Fig. 7. The damage thresholds remain almost constant. These measurements and those performed at different cryostat temperatures indicate that neither the wavelength nor the power density but solely the spot temperature is the critical parameter in the oxygen out-diffusion observed at low residual pressures.

VI. LASER ANNEALING AT HIGH RESIDUAL PRESSURES

In Fig. 8 we show damage thresholds and concomitant maximum spot temperatures of laser-annealing measurements performed at $T_0 = 300$ K and $\lambda_L = 514$ nm for various residual pressures. Although the pressures rise by eight orders of magnitude, the damage threshold remains almost constant. Especially, the temperature thresholds deduced from the damage thresholds rise at most by 40 K, if at all.

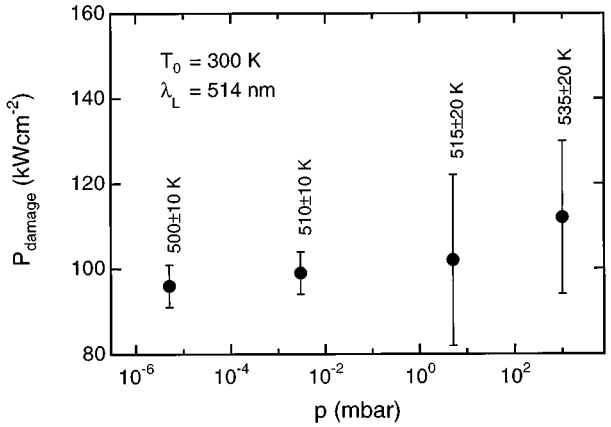

FIG. 8. Damage thresholds vs residual pressure. The corresponding maximum spot temperatures $T_{\max}$ are indicated. The effective spot radius is $r_e = 8.4\ \mu$m.

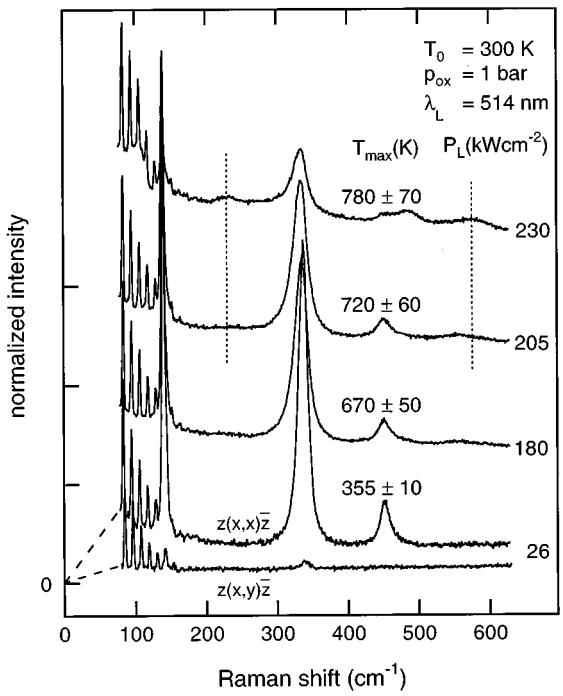

FIG. 9. Polarized Stokes Raman spectra of a laser-annealing measurement for different power densities P_L with an effective spot radius $r_e = 8.3\ \mu$m. Also depicted is a depolarized spectrum taken at the lowest power density $P_L = 26$ kW cm^{-2}. The spectra are offset as indicated. The dotted lines correspond to infrared-active modes of $YBCO_{6.5}$. Also given are the maximum spot temperatures $T_{\max}$.

This is in contrast to the p_{ox}-T phase diagram of $YBCO_{6+x}$ which describes the equilibrium chain-oxygen content x as a function of the oxygen partial pressure p_{ox} and the ambient temperature T.[3] According to the phase diagram the equilibrium temperature for constant x rises by about 400 K within this pressure range when the initial temperature is around 500 K. Furthermore, the Raman spectra taken at the highest power density did not depend on the pressure; i.e., they all indicate that the illuminated area consisits predominantly of tetragonal sites with $x = 0$. However, even before $YBCO_{6+x}$ starts to melt at 1 bar oxyen partial pressure at about 1300 K, the oxygen content expected from the phase diagram is $x = 0.3$. At 900 K and 1 bar oxygen partial pressure an equilibrium oxygen content of $x = 0.7$ would be expected. Hence, the complete oxygen loss cannot be explained by thermal activation. Instead of this, we believe that the laser-anealing measurements on $YBCO_7$ films carried out at higher residual pressures give strong evidence for photon-stimulated desorption of oxygen in the center of the laser spot.

In order to investigate the oxygen in-diffusion we have performed laser-annealing measurements of tetragonal films in 1 bar oxygen. These measurements serve also the purpose to gain further insight into the presumably photon-stimulated desorption of oxygen. Stokes spectra of a typical experiment are presented in Fig. 9. Due to the high oxygen pressure, rotational modes of oxygen are observed in the low-frequency region up to 150 cm^{-1}. At the two lower power densities we observe the three expected phonons of $YBCO_6$,

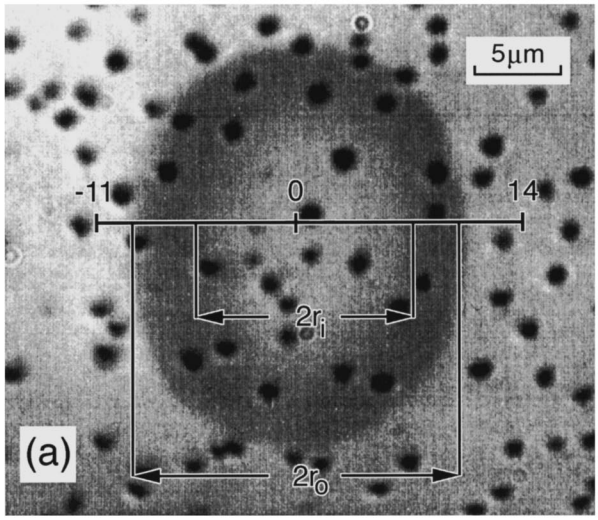

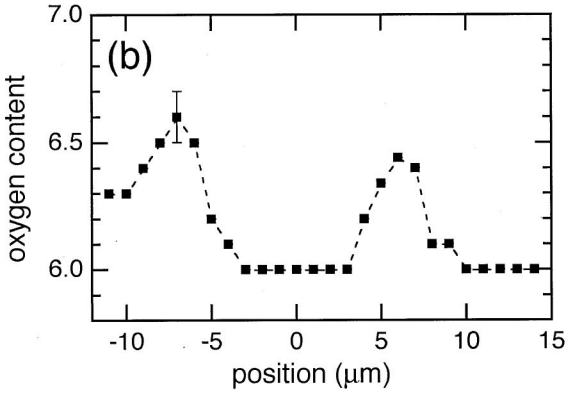

FIG. 10. (a) Optical micrograph of a $YBCO_6$ film after illumination with a power density of $P_L=282$ kW cm^{-2} and an effective spot radius $r_e=8.3$ μm in 1 bar oxygen for 1 s. (b) Local oxygen content determined from an analysis of micro-Raman spectra taken at various sites along the line in (a). A representative error bar is shown for the site 7 μm left from the center.

i.e., the Cu(2) mode at 140 cm^{-1}, the O(2)-O(3) mode at 340 cm^{-1}, and the O(2)+O(3) mode at 450 cm^{-1}.[14] While the spot remains tetragonal for power densities up to 180 kW cm^{-2}, the appearance of disorder-induced modes for higher power densities indicates the onset of oxygen absorption. The spectrum recorded with the highest power density is similar to the corresponding one of Fig. 1. A typical optical micrograph of an illuminated site is given in Fig. 10(a). In the micrograph a dark ring-shaped region with a higher oxygen content is observed on the bright tetragonal film. Therefore, oxygen in-diffusion takes place in regions away from the center whereas the center itself remains tetragonal in agreement with the results obtained on orthorhombic films. Results of micro-Raman investigations of the ring performed in ambient atmosphere are shown in Fig. 10(b). They reveal that within an inner radius $r_i\approx 5$ μm the film is tetragonal, the dark ring-shaped area with an outer radius $r_o\approx 9$ μm has an oxygen content of $x\approx 0.5$, and the other regions remain unaltered.

The spot temperatures for the annealing experiments carried out on tetragonal films cannot be calculated accurately

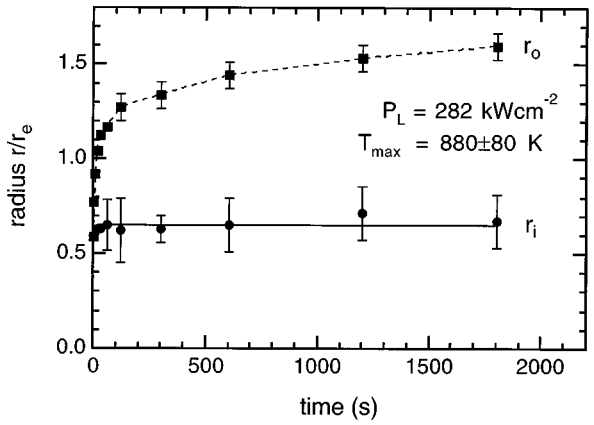

FIG. 11. Normalized inner radius r_i and outer radius r_o of an oxidized $YBCO_6$ film vs exposure time when illuminated with a power density of $P_L=282$ kW cm^{-2}. The measurements have been performed in 1 bar oxygen at a cryostat temperature $T_0=300$ K and a maximum spot temperature $T_{\max}=(880\pm 80)$ K. The radii are normalized with respect to the effective spot radius $r_e=8.3$ μm.

from the heat model, as we cannot measure the thermal boundary resistance of a nonsuperconducting film. The thermal boundary resistance is a consequence of the fact that phonons are refracted at the interface between two media with different phonon band structures.[27] Removing chain oxygen from $YBCO_7$ results in only slight variations of its phonon band structure.[28] Thus, we assume $R_{\rm bd}=(1\pm 0.5)\times 10^{-3}$ K cm^2 W^{-1} which is a typical value of our $YBCO_7$ films. The same argument allows us to use the thermal conductivity of $YBCO_7$ along the c axis for the tetragonal films, as this conductivity is almost entirely due to phonons.[22] With these assumptions we are able to determine the maximum spot temperatures $T_{\max}$ from Eq. (1). They are depicted in Fig. 9. However, the uncertainty of the thermal boundary resistance results in considerable uncertainties of these temperatures.

In order to investigate the time dependence of oxygen absorption and diffusion in the laser-heated film we have illuminated different sites of the tetragonal film with varying exposure times. For these experiments we chose a power density of 282 kW cm^{-2}, i.e., a maximum spot temperature of $T_{\max}=(880\pm 80)$ K where oxygen absorption is observed. The inner and outer radii versus exposure time are given in Fig. 11. While the outer radius grows fast for small exposure times, the growing levels off at longer times. The latter reflects the fact that oxygen in-diffusion as well as lateral diffusion becomes slower in regions away from the center as the temperature is decreasing there. The inner radius r_i remains constant within the error bars; i.e., within the inner radius the photon-stimulated desorption of oxygen exceeds the thermally activated oxygen in-diffusion for any time. The mean value of the observed inner radii is $r_i=5.5$ μm or $r_i=0.66r_e$ for this experiment.

VII. DISCUSSION

Thermally activated diffusion of oxygen in $YBCO_{6+x}$ can be described by Fick's law (see, e.g., Ref. 29)

$$\mathbf{j}_T(\mathbf{x}) = \mathbf{D}\nabla c(\mathbf{x}), \tag{6}$$

where $\mathbf{j}_T(\mathbf{x})$ is the oxygen flux resulting from the concentration gradient $\nabla c(\mathbf{x})$ and $\mathbf{D}$ is the diagonal diffusion tensor. For directions $j = x,y,z$ we have the diffusion coefficients

$$D^j = D_0^j \exp\left[\frac{-E_A^j}{k_B T(\sqrt{x^2+y^2},z)}\right].$$

Here E_A^j and D_0^j are the activation energy and the diffusion constant for diffusion in the j direction, respectively, k_B is the Boltzmann constant, and $T(\sqrt{x^2+y^2},z)$ is the temperature which depends only on $r=\sqrt{x^2+y^2}$ and z for circular laser spots. In the following we describe the concentration gradient by the difference between the equilibrium oxygen content x_{eq} and the initial oxygen content x_0 of the film. The equilibrium content is determined from the p_{ox}-T phase diagram of $YBCO_{6+x}$.[3]

In general, a diffusion process consists of bulk and interface diffusion, where interfaces are, e.g., grain boundaries or surfaces. As the process with the lowest diffusion coefficient will determine the velocity of the reaction, the restriction to a single activation energy as done in Eq. (6) will always give a good description of the diffusion. The bulk diffusion of oxygen in $YBCO_{6+x}$ is highly anisotropic and takes place predominately in the ab plane, especially at temperatures below 670 K.[30] However, c-axis-oriented $YBCO_{6+x}$ films consist of various grains whose mosaic boundaries act as short circuits for oxygen diffusion.[31,32] Typical activation energies for bulk and interface diffusion of oxygen in $YBCO_{6+x}$ are about 1 eV.[33–35] It was observed that activation energies for oxygen out-diffusion are higher than those for oxygen in-diffusion.[36] Furthermore, it was shown that the activation energies decrease with increasing oxygen partial pressure.[37] To give an example, an activation energy of 0.2 eV was reported for the oxygen out-diffusion at 1 bar oxygen partial pressure.[37] In the following we restrict ourself to oxygen in- and out-diffusion from the surface described by effective chemical diffusion coefficients D^{in} and D^{out}. Then, Eq. (6) becomes

$$\mathbf{j}_T^{\mathrm{in/out}}(r) = D^{\mathrm{in/out}} \left.\frac{\partial c(r,z)}{\partial z}\right|_{z=0} \mathbf{e}_z, \tag{7}$$

with

$$D^{\mathrm{in/out}} = D_0^{\mathrm{in/out}} \exp\left[\frac{-E_A^{\mathrm{in/out}}}{k_B T_{\max}(r)}\right]$$

in cylindrical coordinates, where $T_{\max}(r)$ is the temperature at the film surface (see Sec. IV).

At low oxygen partial pressure and sufficiently high temperature oxygen will desorb from a $YBCO_7$ film. At the surface oxygen out-diffusion has already been observed at room temperature with time scales of several hours.[5] Oxygen from the bulk will follow the concentration gradient to the surface if its mobility is high enough, i.e., if the local temperature is high enough. According to our experiments this is the case for temperatures above 490 K. Then oxygen will flow in the bulk and desorb from the surface from regions close to the spot center. The new profile of the oxygen content establishes very fast, as we did not observe variations in subsequent spectra which were taken after an initial illumination of 3 min. Hence, the local oxygen content is already in thermal equilibrium after that time. With increasing spot temperature the region around the spot center in which oxygen rearrangement takes place grows. This region can be described by a mean oxygen content $x \approx 0.5$. When the spot temperature exceeds 580 K the oxygen content within the penetration depth has decreased to $x=0$.

In the above-discussed experiments the oxygen desorption seems to be temperature induced. However, several investigations have shown that oxygen out-diffusion in vacuum can be neglected for temperatures below 670 K.[29,36,37] The slow out-diffusion is mainly determined by the desorption process, as oxygen in the bulk becomes remarkably mobile already at room temperature, provided the oxygen content is below $x=1$.[38–40] The short time scale of the desorption observed in our experiments already at 490 K could be related to photon-stimulated desorption of oxygen at the surface.

Photon-stimulated desorption (PSD) of oxygen from the surface can be described by a flux

$$\mathbf{j}_{\mathrm{PSD}}(r) = -C_\omega P_L \exp\left(-\frac{r^2}{r_e^2}\right)\mathbf{e}_z, \tag{8}$$

with the power density $P_L = \dot{n}\hbar\omega$. Here $\dot{n}$ is the photon flux density and C_ω is proportional to the cross section of the desorption. The cross section will depend on the photon energy as well as on the energy barrier involved in the photoactivated process. The fact that we did not observe a dependence of the damage threshold on the photon energy indicates that this energy barrier would be below 2.41 eV. Photon-stimulated desorption has been observed in experiments on $DyBCO_7$ samples with synchrotron radiation of high flux densities and energies down to 10 eV.[7] The authors explain their observations by core-level excitations which lead to oxygen desorption and suggest that shallow core levels of Ba($5p$) at 17 eV and of O($2s$) at 22 eV are involved in these processes. Desorption occurring at lower energies is explained in terms of second-order light. As our laser energies are far below these values this process cannot account for the desorption in our experiments. On the other hand photon-stimulated desorption was also observed in optical-activated isotope exchange experiments in ZnO.[41] In these samples the maximum in the desorption efficiency has been related to excitonic excitations. Indeed, electronic excitations in the visible regime have been observed in luminescence spectra of $YBCO_{6+x}$.[42,43] They have been related to photogeneration of charges which play an important role in the persistent photoconductivity.[43] The latter authors suggest that oxygen vacancies in the Cu(1)-O(1) chains act as F centers which trap photoexcited electrons. These F centers may play a similar role in the desorption of oxygen from the surface as excitons do in ZnO. It is worthwhile to mention that persistent photoconductivity is a bulk effect. Therefore, it is not clear whether the oxygen vacancies at the surface will behave in a similar way than those in the bulk. Photon-stimulated desorption at the surface was observed when oxygen monolayers adsorbed on Pt(111) were irradiated with photons whose energy exceeded 2.7 eV.[44] These authors explain the observed desorption efficiency with excitations of the adsorbed oxygen molecules whose frontier orbitals split

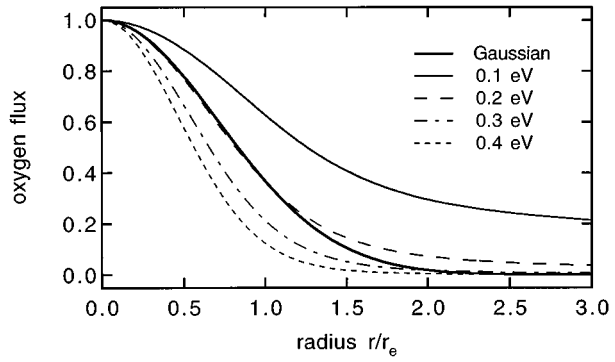

FIG. 12. Normalized lateral distributions of the thermally activated oxygen flux into the $YBCO_6$ film calculated from Eq. (7) for parameters $T_0=300$ K, $p_{ox}=1$ bar, $T_{max}=880$ K, and various activation energies E_A^{in}. For comparison a normalized Gaussian profile which represents photon-stimulated desorption is given.

due to interactions with Pt *d* orbitals. Whether this orbital splitting will also occur on $YBCO_{6+x}$ surfaces and if so whether the energy threshold will be below 2.41 eV have not been investigated so far.

At an oxygen partial pressure of 1 bar thermally activated oxygen in- and out-diffusion has already been observed at low temperatures of 500 K.[34,45] The equilibrium oxygen content at this pressure is above $x=0.7$ when the temperature is below 900 K.[3] From this we expect that even at the highest power density thermally activated desorption plays a minor role in our experiments on $YBCO_7$ films. Therefore, we explain the fact that oxygen-depleted areas with $x=0$ are observed in laser-annealing measurements by photon-stimulated desorption of oxygen which occurs predominately in the center of the Gaussian laser spot. Measurements performed on $YBCO_6$ films in 1 bar oxygen helped us to distinguish regions where thermally activated oxygen in-diffusion and photon-stimulated desorption is observed, respectively. According to Eq. (8) the desorption will have a Gaussian profile. The observed ring-shaped oxidized region depicted in Fig. 10 demonstrates that the lateral profile of the thermally activated oxygen flux falls off slower than a Gaussian function. Consequently, in regions far from the center the thermally activated oxygen in-diffusion dominates the photon-stimulated desorption and vice versa. At the inner radius r_i the oxygen fluxes due to both processes compensate, i.e., $\mathbf{j}_T^{in}(r_i)=-\mathbf{j}_{PSD}(r_i)$. As the temperature profile develops very rapidly we do not see any time dependence of the inner radius in Fig. 11.

The lateral profile of the thermally activated oxygen flux can be calculated according to Eq. (7). In this calculation the lateral temperature distribution at the film surface discussed in Sec. IV has to be considered. For a given temperature distribution the profile of the oxygen flux is a sensitive function of the activation energy E_A^{in}. In Fig. 12 we show profiles for activation energies $E_A^{in}=$ 0.1, 0.2, 0.3, and 0.4 eV considering $T_{max}=880$ K as in the experiments depicted in Figs. 10 and 11. These profiles are compared to a Gaussian function. The data show that the activation energy of oxygen in-diffusion must be below 0.3 eV in order to obtain sufficiently flat profiles of the thermally activated oxygen flux at radii higher than r_e. A detailed analysis where we have considered the experimentally observed inner radius $r_i=0.66r_e$ yields an upper bound of the activation energy $E_A^{in}<(0.19\pm0.01)$ eV. Interestingly, such low activation energies are normally observed in the case of oxygen in-diffusion in polycrystalline specimens, whereas single crystals are shown to have activation energies above 1 eV.[36] This demonstrates that grain-boundary diffusion plays an important role in the thermally activated oxygen in-diffusion into $YBCO_{6+x}$ films.

VIII. CONCLUSION

In the first part of this work we investigated the behavior of $YBCO_7$ films when annealed with a laser beam of high power at low residual pressures. Analysis of the spectra and of the laser-annealed site, as well as laser-annealing measurements performed at different cryostat temperatures, allowed us to develop a simple picture of the process of the oxygen out-diffusion under these conditions. According to this picture oxygen starts to diffuse out of the film when the maximum spot temperature reaches 490 K. With increasing spot temperature the region around the spot center in which a new oxygen concentration profile establishes grows. This region can be described by a mean oxygen content $x\approx0.5$. When the maximum spot temperature exceeds 580 K the oxygen content within the penetration depth decreases to $x=0$.

In the second part we presented laser-annealing measurements performed at higher residual pressures. In measurements on $YBCO_7$ films carried out in 1 bar oxygen we observed tetragonal spot centers ($x=0$) at high power densities. This is not expected in a thermally activated process. According to the p_{ox}-T phase diagram the minimum oxygen content of $YBCO_{6+x}$ is above $x=0.3$ even before the material starts to melt at this pressure. Investigations of $YBCO_6$ films in 1 bar oxygen were used to study oxygen in-diffusion. We observed that ring-shaped oxidized regions appear at high power densities.

In the last part of this work we showed that oxygen out-diffusion from $YBCO_7$ films at low residual pressure may well be explained by thermally activated bulk diffusion and photon-stimulated desorption of oxygen from the surface. Photon-stimulated desorption could also account for the observed tetragonal spot centers at high residual pressures up to 1 bar oxygen and the ring-shaped oxidized regions, observed when $YBCO_6$ films are investigated in 1 bar oxygen. These rings can be described as a result of competing oxygen fluxes due to thermally activated oxygen in-diffusion and photon-stimulated desorption. In particular, it turned out that the activation energy for the thermally activated process must be below $E_A^{in}=(0.19\pm0.01)$ eV in order to obtain lateral profiles of the thermally activated oxygen flux which fall off slower than the Gaussian distribution of the power density.

The underlying mechanism of the photon-stimulated desorption could not be identified so far. As our investigations were performed in the visible regime we can rule out that core-level excitations of Ba($5p$) and O($2s$) lead to oxygen desorption which has been suggested as a mechanism in the case of $DyBCO_7$ samples irradiated with synchrotron radiation of high intensity. There are two other mechanisms

which may account for photon-stimulated desorption of oxygen. One has been investigated on polycrystals of ZnO, where excitonic excitations have been related to the spectral dependence of the desorption efficiency. Another has been investigated on oxygen monolayers adsorbed on Pt(100) surfaces, where excitations of frontier orbitals of adsorbed oxygen which split due to interactions with surface atoms are related to the spectral dependence of the desorption efficiency.

ACKNOWLEDGMENT

This work was supported by the Bundesministerium für Forschung und Technologie, Federal Republic of Germany, under Contract No. 13N5807A.

[1] Z. Z. Wang, J. Clayhold, N. P. Ong, J. M. Tarascon, L. H. Greene, W. R. McKinnon, and G. W. Hull, Phys. Rev. B **36**, 7222 (1987).

[2] H. Claus, M. Braun, A. Erb, K. Röhberg, B. Runtsch, H. Wühl, G. Bräuchle, P. Schweib, G. Müller-Vogt, and H. v. Löhneysen, Physica C **198**, 42 (1992).

[3] R. E. Somekh and Z. H. Barber, in *Physics and Materials Science of High Temperature Superconductors II*, edited by R. Kossowsky *et al.* (Kluwer Academic Publishers, Dordrecht, Netherlands, 1992), p. 443.

[4] See, e.g., J. D. Jorgensen, B. W. Veal, W. K. Kwok, G. W. Crabtree, A. Umezawa, L. J. Nowicki, and A. P. Paulikas, Phys. Rev. B **36**, 5731 (1987); C. Greaves and P. R. Slater, Solid State Commun. **74**, 591 (1990).

[5] T. J. Wagener, Y. Gao, J. H. Weaver, A. J. Arko, B. Flandermeyer, and D. W. Carpone II, Phys. Rev. B **36**, 3899 (1987).

[6] B. H. Moeckly, R. A. Buhrman, and P. E. Sulewski, Appl. Phys. Lett. **64**, 1427 (1994).

[7] R. A. Rosenberg and C.-R. Wen, Phys. Rev. B **39**, 6630 (1989).

[8] See, e.g., R. R. Krchnavek, S.-W. Chan, C. T. Rogers, F. DeRosa, M. K. Kelly, P. F. Miceli, and S. J. Allen, J. Appl. Phys. **65**, 1802 (1989); R. C. Dye, R. E. Muenchausen, N. S. Nogar, A. Mukherjee, and S. R. J. Brueck, Appl. Phys. Lett. **57**, 1149 (1990); Y. Q. Shen, T. Freltoft, and P. Vase, *ibid.* **59**, 1365 (1991); R. Sobolewski, W. Xiong, and W. Kuala, IEEE Trans. Appl. Supercond. **AS-3**, 2986 (1993).

[9] A. Bock, Phys. Rev. B **51**, 15 506 (1995). In this work we use an anti-Stokes correction factor $C_{AS}=1.1$.

[10] M. Schilling, F. Goerke, and U. Merkt, Thin Solid Films **235**, 202 (1993).

[11] K. F. McCarty, J. Z. Liu, R. N. Shelton, and H. B. Radousky, Phys. Rev. B **41**, 8792 (1990).

[12] N. Dieckmann, R. Kürsten, M. Löhndorf, and A. Bock, Physica C **245**, 212 (1995).

[13] R. Feile, Physica C **159**, 1 (1989).

[14] G. Burns, F. H. Dacol, C. Feild, and F. Holtzberg, Physica C **181**, 37 (1991).

[15] D. R. Wake, F. Slakey, M. V. Klein, J. P. Rice, and D. M. Ginsberg, Phys. Rev. Lett. **67**, 3728 (1991).

[16] C. Thomsen, A. P. Litvinchuk, E. Schönherr, and M. Cardona, Phys. Rev. B **45**, 8154 (1992).

[17] M. Iliev, C. Thomsen, V. Hadjiev, and M. Cardona, Phys. Rev. B **47**, 12 341 (1993).

[18] E. T. Heyen, J. Kircher, and M. Cardona, Phys. Rev. B **45**, 3037 (1992).

[19] N. Dieckmann, A. Bock, and U. Merkt, Physica C **244**, 35 (1995).

[20] J. Kircher, M. K. Kelly, S. Rashkeev, M. Alouani, D. Fuchs, and M. Cardona, Phys. Rev. B **44**, 217 (1991). From an analysis of Figs. 3–5 we obtain $l=73$ nm and $R=13\%$ for $\lambda_L=514$ nm and $x=1$, and $l=92$ nm and $R=16\%$ for $\lambda_L=514$ nm and $x=0$.

[21] L. J. Challis, A. M. de Goër, K. Guckelsberger, and G. A. Slack, Proc. R. Soc. London A **330**, 29 (1972).

[22] S. J. Hagen, Z. Z. Wang, and N. P. Ong, Phys. Rev. B **40**, 9389 (1989).

[23] M. Lax, J. Appl. Phys. **48**, 3919 (1977).

[24] B. Friedl, C. Thomsen, H.-U. Habermeier, and M. Cardona, Solid State Commun. **78**, 291 (1991).

[25] E. T. Heyen, S. N. Rashkeev, I. I. Mazin, O. K. Andersen, R. Liu, M. Cardona, and O. Jepsen, Phys. Rev. Lett. **65**, 3048 (1990).

[26] M. Nahum, S. Verghese, P. L. Richards, and K. Char, Appl. Phys. Lett. **59**, 2034 (1991).

[27] W. A. Little, Can. J. Phys. **37**, 334 (1959).

[28] W. Reichardt, N. Pyka, L. Pintschovius, B. Hennion, and G. Collin, Physica C **162-164**, 464 (1989).

[29] K. N. Tu, N. C. Yeh, S. I. Park, and C. C. Tsuei, Phys. Rev. B **39**, 304 (1989).

[30] S. I. Bredikhin, G. A. Emel'chenko, V. S. Shechtman, A. A. Zhokhov, S. Carter, R. J. Chater, J. A. Kilner, and B. C. H. Steele, Physica C **179**, 286 (1991).

[31] Y. X. Chen, J. Zhang, and Z. Wu, Supercond. Sci. Technol. **5**, 463 (1992).

[32] Y. Li, J. A. Kilner, T. J. Tate, M. J. Lee, R. J. Chater, H. Fox, R. A. De Souza, and P. G. Quincey, Phys. Rev. B **51**, 8498 (1995).

[33] R. K. Siddique, Z. Phys. B **93**, 411 (1994).

[34] C. Krüger, K. Conder, and E. Kaldis, Physica C **213**, 219 (1993).

[35] X. M. Xie, T. G. Chen, and Z. L. Wu, Phys. Rev. B **40**, 4549 (1989).

[36] J. R. LaGraff and D. A. Payne, Phys. Rev. B **47**, 3380 (1993).

[37] J. R. LaGraff and D. A. Payne, Physica C **212**, 478 (1993).

[38] P. Gerdanian, C. Picard, and B. Touzelin, Physica C **182**, 11 (1991).

[39] B. W. Veal, A. P. Paulikas, H. You, H. Shi, Y. Fang, and J. W. Downey, Phys. Rev. B **42**, 6305 (1990).

[40] V. G. Hadjiev, C. Thomsen, J. Kircher, and M. Cardona, Phys. Rev. B **47**, 9148 (1993).

[41] V. S. Tkalich and A. A. Lisachenko, Sov. J. Chem. Phys. **6**, 1264 (1990).

[42] V. G. Stankevitch, N. Y. Svechnikov, K. V. Kaznacheev, M. Kamada, S. Tanaka, S. Hirose, R. Kink, G. A. Emel'chenko, S. G. Karabachev, T. Wolf, H. Berger, and F. Levy, Phys. Rev. B **47**, 1024 (1993).

[43] J. F. Federici, D. Chev, B. Welker, W. Savin, J. Gutierrez-Solana, T. Fink, and W. Wilber, Phys. Rev. B **52**, 15 592 (1995).

[44] X.-Y. Zhu, S. R. Hatch, A. Campion, and J. M. White, J. Chem. Phys. **91**, 5011 (1989).

[45] K. Conder, E. Kaldis, M. Maciejewski, K. A. Müller, and E. F. Steigmeier, Physica C **210**, 282 (1993).